

<https://doi.org/10.1038/s43247-026-03292-7>

# Tripole-like Antarctic sea ice pattern linked to remote forcing from the Indian Ocean and Maritime Continent

Check for updates

Weihan Ma<sup>1,2</sup>, Xiaojun Yuan<sup>3</sup>, Yurong Hou<sup>1,2</sup>, Kai Man<sup>4</sup>, Yujie Miao<sup>1,2</sup>, Li Zhang<sup>5,6</sup> & Xichen Li<sup>6,7</sup>

Antarctic sea ice variability has long been characterized by a dipole pattern primarily located in West Antarctica, attributed to the Amundsen Sea Low and remote forcing from the tropical Pacific, while variability in other sectors has received less attention. Here we reveal a tripole-like pattern of sea ice variability spanning multiple sectors of Antarctica, comprising the classic dipole together with seasonally varying centers in East Antarctica during austral winter and spring. Using observational analyses and numerical experiments, we demonstrate that, unlike the dipole, this tripole is not governed solely by the Amundsen Sea Low. Instead, it emerges from paired atmospheric circulation anomalies that impose coherent wind forcing along the sea ice edge, initiated by Rossby wave trains from the Pacific, Indian Ocean and Maritime Continent. These findings provide a broader framework for Antarctic sea ice variability and highlight previously overlooked Indian Ocean-Maritime Continent drivers of Antarctic climate predictability.

The dipole sea ice pattern has been recognized as the dominant mode of the inter-annual Antarctic sea ice variability, manifesting as seesaw-like sea-ice anomalies between the Ross-Amundsen Seas and Bellingshausen-Weddell Seas around West Antarctica<sup>1,2</sup>. Despite this, the inter-annual variability of Antarctic sea ice exhibits pronounced regional differences, and emerging evidence suggests that variability in East Antarctic sea ice, particularly in regions west of the Ross Sea and east of the Weddell Sea, may rival the variability observed in the West Antarctic<sup>3,4</sup>. These regions exhibit variability of a similar magnitude to the Antarctic Dipole<sup>5,6</sup>, emphasizing the necessity of investigating the broader spatial distribution and seasonal dynamics of the pan-Antarctic sea ice variability.

The inter-annual variability of the Antarctic sea ice, in particular the sea ice dipole pattern, is considered to be driven by the local atmospheric dynamics, such as the Amundsen Sea Low (ASL)<sup>7–10</sup>. The ASL represents the most prominent low-pressure center associated with leading modes of Southern Hemisphere atmospheric variability: the Southern Annular Mode (SAM)<sup>11,12</sup>. Anomalous shallowing of the ASL drives the Antarctic Dipole through opposing thermal advection<sup>8,13,14</sup> and mechanical forcing<sup>7,15</sup>. Furthermore, other circulation centers associated with the SAM may also influence Antarctic sea ice patterns<sup>6,16</sup>. These centers are interconnected by Rossby wave dynamics, emphasizing the potential for examining Antarctic

sea ice variability through the lens of linked circulation centers across the continent, rather than limiting analyses to West Antarctica and ASL.

While these atmospheric circulation centers around Antarctica drive the redistribution of Antarctic sea ice, they are further modulated by tropical-polar teleconnections<sup>17,18</sup>, with sea surface temperature (SST) variability across all three tropical ocean basins serving as key triggers. These teleconnections, triggered by tropical variability, propagate to the high-latitude Southern Hemisphere through Rossby wave dynamics. The propagation pathway depends strongly on the atmospheric mean flow<sup>19–21</sup>. In particular, the subtropical jet serves as a waveguide and barrier to these wave trains: the intensified anticyclonic curvature on its poleward flank creates a channel of stationary wave trains toward Antarctica<sup>22,23</sup>. Seasonal variations in the subtropical jet alter the pathway of these wave trains by changing their strength and phase<sup>24,25</sup>. This seasonality becomes especially pronounced during austral winter and spring when the jet is stronger<sup>26</sup>. The enhanced jet structure allows Rossby wave activity from the tropics to propagate more efficiently into high latitudes, further seasonally impacting Antarctic sea ice variability.

Building on this general framework, previous studies have identified several specific teleconnection pathways linking individual tropical basins to Antarctica. The Pacific-Antarctic teleconnections, driven by El Niño/

<sup>1</sup>Institute of Atmospheric Physics, Chinese Academy of Sciences, Beijing, China. <sup>2</sup>University of Chinese Academy of Sciences, Beijing, China. <sup>3</sup>Lamont-Doherty Earth Observatory of Columbia University, New York, NY, USA. <sup>4</sup>Frontiers Science Center for Deep Ocean Multispheres and Earth System and Key Laboratory of Physical Oceanography/Academy of the Future Ocean, Ocean University of China, Qingdao, China. <sup>5</sup>Laoshan Laboratory, Qingdao, China. <sup>6</sup>Institute of Ocean Research, School of Physics, Peking University, Beijing, China. <sup>7</sup>Department of Atmospheric and Oceanic Sciences, School of Physics, Peking University, Beijing, China. ✉e-mail: zhangli@ouc.edu.cn; xichenli@pku.edu.cn

Southern Oscillation (ENSO)-related tropical atmospheric deep convection<sup>27,28</sup>, have been the most extensively investigated<sup>22,29–31</sup>. The ENSO-induced stationary Rossby wave train, referred to as the Pacific South America pattern<sup>32,33</sup>, propagates southeastward to Antarctica<sup>34</sup>, interacting with the ASL to amplify the Antarctic Dipole around West Antarctica<sup>23,35</sup>. Similarly, warm SST anomalies in the tropical Atlantic can deepen the ASL through poleward-propagating Rossby wave trains<sup>24,36</sup>. While these Pacific and Atlantic influences predominantly affect West Antarctic sea ice, emerging evidence shows that the Indian Ocean can modulate not only West Antarctica but also East Antarctica<sup>4,37,38</sup>, with its impacts strengthening during austral winter and spring.

Despite recent progress, our understanding of Antarctic sea-ice variability remains incomplete. While the Antarctic Dipole is widely recognized as the leading mode of interannual variability driven primarily by ENSO, the pronounced seasonality of tropical–Antarctic teleconnections, together with growing evidence for Indian Ocean influence, raises the prospect that East Antarctic sectors may host variability centers of comparable magnitude during specific seasons. This has not yet been systematically explored. Moreover, even if such seasonally dependent centers exist, it remains unclear how concurrent forcing from multiple tropical basins combines to shape Antarctic sea-ice variability, and how individual basins contribute to the resulting patterns. These unresolved questions motivate our examination of the dominant sea-ice variability mode in each season and the basin-specific tropical–Antarctic pathways that generate these patterns.

Here, we investigate the seasonal differences in the inter-annual variability of the pan-Antarctic sea ice and its linkage to local atmospheric circulation and remote tropical forcing. Our results reveal a tripole-like sea ice pattern in both austral winter and spring, characterized by a distinct seasonal displacement in spatial structure. While the well-known Antarctic

Dipole is primarily driven by ENSO-related ASL variability, the sea ice tripole is more closely linked to the positioning of atmospheric “circulation pairs.” This circulation pattern consists of three pressure centers that regulate surface winds near the sea ice edge and generate pronounced sea ice anomalies in each season. Importantly, these circulation structures are modulated by seasonally distinct Rossby wave trains originating from different regions of the tropical Indo-Pacific, underscoring the pivotal role of tropical–polar teleconnections in shaping Antarctic sea ice variability.

## Result

### Structure and seasonal differences of the Antarctic sea ice tripole

The dominant inter-annual variability of Antarctic sea ice is characterized by the Antarctic Dipole, defined by the first mode of empirical orthogonal function (EOF) decomposition<sup>1,2</sup> of the Southern Ocean sea ice (Fig. 1) (see “EOF analysis” in “Methods”). The Antarctic Dipole represents a seesaw-like pattern between the Ross–Amundsen and Bellingshausen–Weddell Seas (box I–II in Fig. 1a), mainly centered over the ocean sectors around West Antarctica. This sea ice variability is primarily driven by the local atmospheric circulation through thermal advection and mechanical forcing<sup>8,13,14</sup>, and is further linked to tropical ocean variability through atmospheric teleconnection<sup>17,18</sup>.

To better clarify the seasonal differences of this dipole pattern, we conducted a similar EOF analysis for all four seasons. Results show distinct features across different seasons: autumn (March–April–May, MAM; Fig. 1c) is the only season that shows a clear dipole-like sea ice pattern, while the leading mode of sea ice variability in summer (December–January–February, DJF; Fig. 1b) exhibits a basin-scale uniform feature, representing an increase (or decrease) of the Antarctic sea ice across the entire Southern Ocean. Interestingly, the main feature of the leading sea ice mode for austral

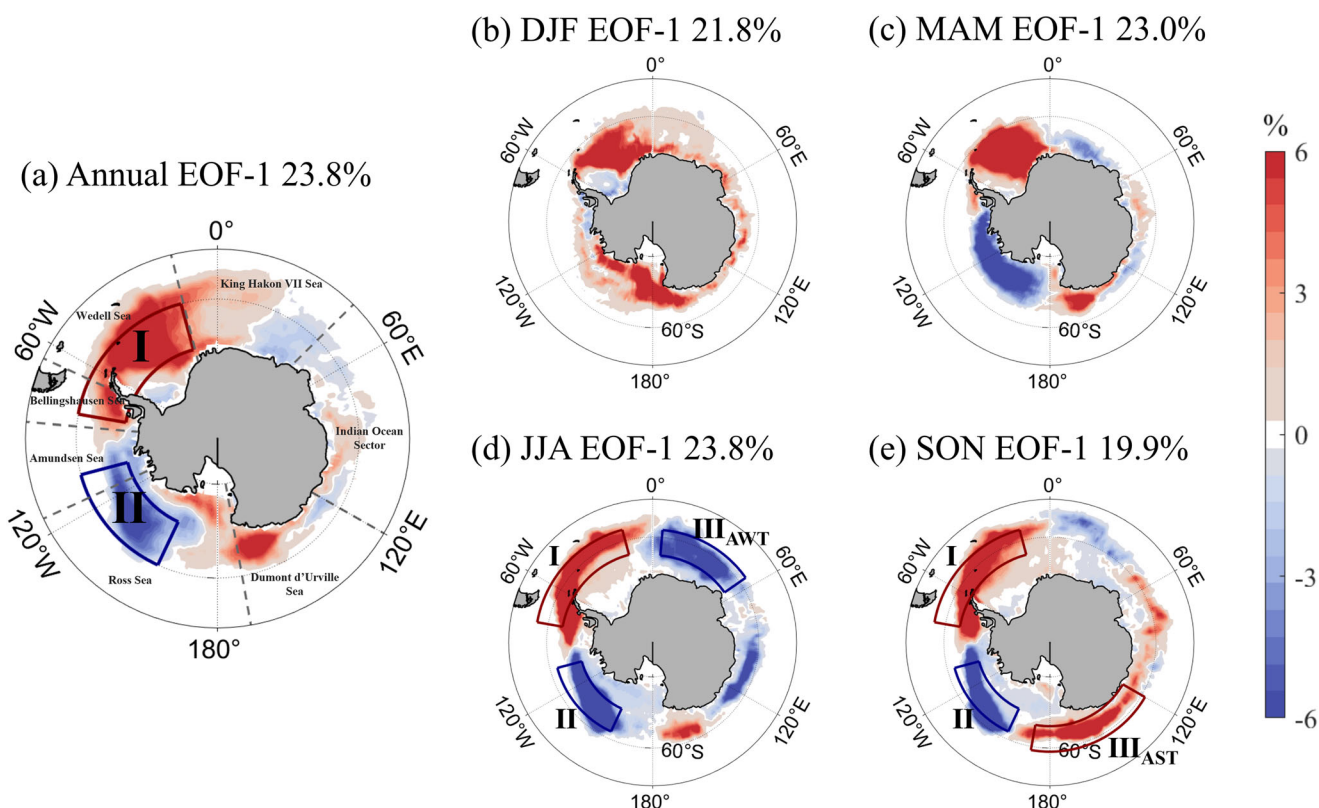


**Fig. 1 | Seasonal differences in the inter-annual variability of the Antarctic sea ice tripole. a–e** First EOF mode of sea ice edge anomalies (30% sea ice concentration, SIC) around Antarctica for the period 1979–2023 (see “EOF analysis” in Methods). The anomalies are shown for **a** annual, **b** austral summer (December–January–February, DJF), **c** autumn (March–April–May, MAM), **d** winter (June–July–August,

JJA), and **e** spring (September–October–November, SON). The red boxes I and blue boxes II highlight the traditional Antarctic Dipole structure in (a), while the boxes III in (d, e) represent the emerging Antarctic sea ice Winter Tripole (AWT) and the Antarctic sea ice Spring Tripole (AST) patterns, respectively.

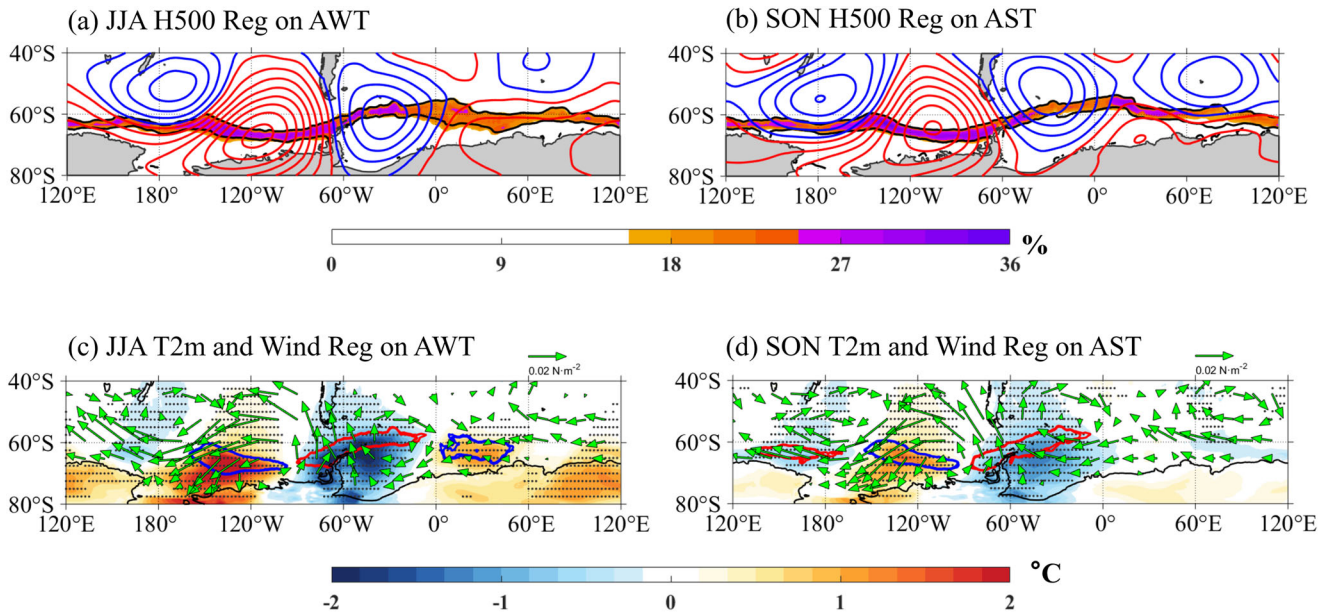


**Fig. 2 | Local circulation pairs controlling the Antarctic sea ice tripole.** Regressions of 500 hPa geopotential height (H500; contours at 6 gpm intervals) against the AWT index during JJA (a) and against the AST index during SON (b). Black contours denote the 10 and 80% seasonal-mean SIC, and shading indicates regions where the SIC standard deviation exceeds 22%. Regressions of 2 m-temperature (T2m; shading) and wind stress (green arrows) against the AWT during JJA (c) and against the AST index during SON (d). Red (blue) contours indicate positive (negative) SIC anomalies of +5% (−5%) in Fig. 1 d, e. Stippling in c, d represents the areas with statistically significant regression coefficients at a level of <5% based on Student’s *t* test.

winter (June–July–August, JJA; Fig. 1d) and spring (September–October–November, SON; Fig. 1e) both display tripole-like patterns that extend into other ocean sectors beyond West Antarctica, hereafter referred to as the Antarctic sea ice Winter Tripole (AWT) and the Antarctic sea ice Spring Tripole (AST), respectively. The AWT, explaining 23.8% of wintertime sea ice variance, is characterized by a classic Antarctic Dipole pattern (box I–II in Fig. 1d), alongside a newly identified negative sea ice anomaly center in the King Hakon Sea (box III<sub>AWT</sub> in Fig. 1d). Similarly, the AST, accounting for 19.9% of the interannual variance in SON, features dipole-like anomalies (box I–II in Fig. 1e) and a pronounced positive anomaly center over the Dumont d’Urville Sea (III<sub>AST</sub> in Fig. 1e).

These observed anomaly centers of the Antarctic tripole (box I–III in Fig. 1d, e) may be partially influenced by the internal sea ice variability. To illustrate the spatial distribution of this variability, we examine the mean values (Supplementary Fig. 1a, b) and standard deviations (Supplementary Fig. 1c, d) of SIC during austral winter and spring. In particular, we highlight the transitional belts where SIC ranges from 10 to 80%, delineated by black contours. Notably, the anomaly centers of the Antarctic tripole (box I–III in Supplementary Fig. 1c, d) tend to align with these transitional belts, which feature a strong SIC gradient and large SIC standard deviations.

Given that the transitional belts are highly sensitive to atmospheric forcing<sup>39,40</sup>, it is essential to examine the role of local atmospheric circulation in shaping the tripole-like sea ice patterns and the seasonal displacement of the third anomaly center (box III in Fig. 1d, e).

**Atmospheric circulation adjustment associated with the Antarctic sea ice tripole**

We define the principal component time series of the JJA and SON leading EOF modes as the AWT and AST indices, respectively (see “EOF analysis” in “Methods”). The regression fields are obtained by regressing each atmospheric variable at every grid point onto these indices. The resulting patterns show that both the AWT (Fig. 2a) and AST (Fig. 2b) are associated with “circulation pairs” exhibiting a low-high-low anomaly pattern of the 500 hPa geopotential height (GPH). Specifically, two low-pressure centers are located over the western Ross Sea and Weddell Sea, while a high-pressure center is situated in the Amundsen Sea. The centers of these

“circulation pairs” lie on, or are situated close to, the transitional belts (color shading in Fig. 2a, b), where the associated wind anomalies cut across these sensitive transition zones, indicating that atmospheric circulation is strongly correlated with regional sea-ice anomalies.

The local circulation regulates sea ice redistribution primarily through thermal advection<sup>8,13,14</sup> and mechanical forcing<sup>7,15</sup>, particularly during the growth and maximum ice periods<sup>41</sup>. In JJA (Fig. 2a, c), the warm and cold advection associated with the shallowing of the ASL increase sea ice over the Bellingshausen–Weddell Seas while decreasing sea ice over the Ross–Amundsen Seas, forming the well-established ADP<sup>1,42</sup> (Fig. 1a). Additionally, anomalous northeasterly winds east of the Weddell Sea Low advect warm air from the South Atlantic into the King Hakon Sea sector, heating the surface (orange shading in Fig. 2c). This onshore wind (green arrows in Fig. 2c) and its associated warm advection reduce SIC (blue contours), forming the third anomaly center in winter (box III in Fig. 1d). In contrast, the anomalous circulation center near the western Ross Sea (Fig. 2a) lies farther north of the transitional belt. As a result, the associated southeasterly winds (green arrows in Fig. 2c) remain weak, limiting cold air advection and failing to create the sea ice anomaly center.

In austral spring, the low-pressure center over the Weddell Sea shifts equatorward (Fig. 2b), while that over the western Ross Sea moves poleward relative to JJA (Fig. 2a). The disappearance of the King Hakon Sea anomaly center is attributed to weakened local wind stress (green arrows in Fig. 2d), caused by the northward shift of anomalous circulation. Meanwhile, the poleward-displaced low over the Ross Sea places its southwestern flank over the transitional belt in the Dumont d’Urville sector. The resulting enhanced southeasterly winds (green arrows in Fig. 2d) advect polar air into this region (blue shading), cooling the surface and increasing SIC (red contour), thereby forming a new anomaly center (box III in Fig. 1e).

Strong meridional winds across the sea ice transitional belt are crucial for generating pronounced SIC anomalies, whereas weak winds produce weak responses. Although three atmospheric pressure anomaly centers occur in both seasons, only the two aligned with transitional belts generate robust meridional winds, leading to two stable sea ice anomaly centers, while the third remains variable. This highlights the tight coupling between local atmospheric dynamics and sea ice variability. Because these “circulation

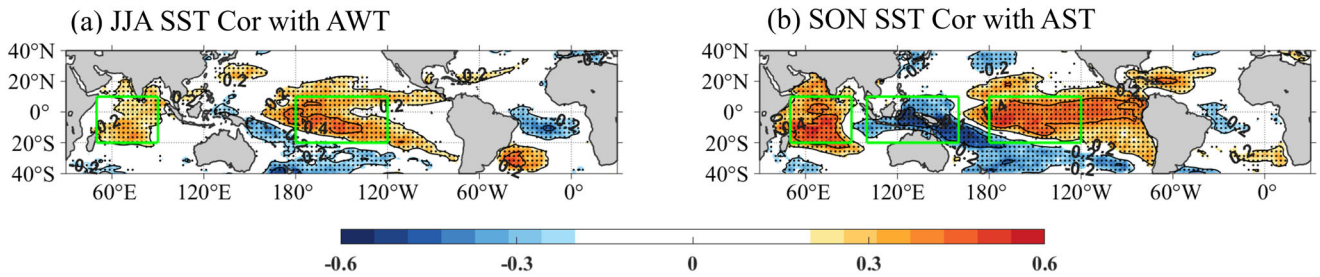


**Fig. 3 | Linkage between the Antarctic sea ice tripole and Indo-Pacific SST variability.** Correlations between tropical sea surface temperature (SST) and the AWT index during JJA (a) and the AST index during SON (b). The Indian Ocean (IO), Maritime Continent (MC) and Pacific Ocean (PO) SST indices are calculated as area-weighted SST averages over the IO region (left green boxes in (a, b)

40°E–110°E, 20°S–10°N), MC region (middle green boxes in (b) 100°E–160°E, 20°S–10°N) and PO region (right green boxes in (a, b) 180°–120°W, 20°S–10°N), respectively. Stippling represents the areas with statistically significant regression coefficients at a level of <5% based on Student’s *t*-test.

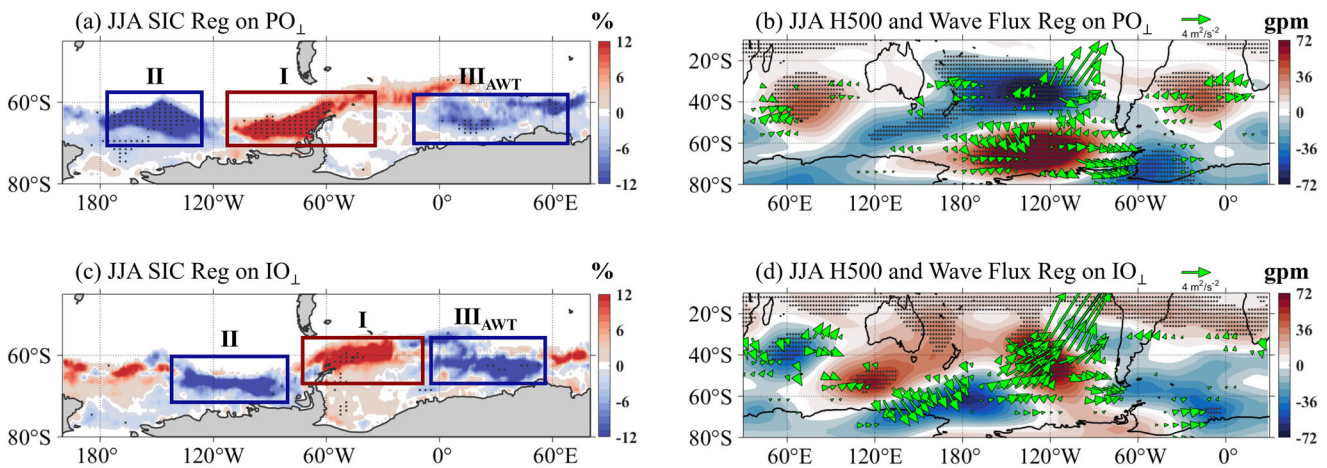


**Fig. 4 | Distinct Rossby wave trains from the Indo-Pacific Oceans modulating the Antarctic sea ice tripole during austral winter.** Partial regressions of (a) SIC (shading) and (b) H500 (shading) and Plumb wave flux (arrows) against the independent  $PO_{\perp}$  index during JJA. c, d are the same as a, b but for the  $IO_{\perp}$  index (see “Partial regression analysis” in “Methods”). The anomalies represent the response to

a 1° variation in these SST indices. Stippling represents the areas with statistically significant regression coefficients at a level of <5% based on Student’s *t*-test. Boxes I–III highlight the development of the wintertime Antarctic sea ice tripole under both PO and IO forcing.

pairs” reflect the impact of mid-latitude Rossby wave trains—often initiated by tropical ocean forcing—the next section examines how tropical-polar teleconnections shape these patterns.

**Teleconnections linking tropical Indo-Pacific variability and the Antarctic sea ice tripole**

Correlation analysis reveals statistically significant associations between the Antarctic sea ice Winter Tripole (Fig. 3a) and Spring Tripole (Fig. 3b) with SST variability across Indo-Pacific basins. In both JJA and SON, the Antarctic tripole patterns are typically linked to a broad warming signal in the central–western Indian Ocean, accompanied by El Niño-like SST anomaly over the central-Pacific Ocean (Fig. 3a, b). In SON, in addition to the signals from the Indian Ocean and central-Pacific, a significant negative correlation emerges over the Maritime Continent. This forms a tripole SST structure, which is an intrinsic mode across the tropical Indo-Pacific region<sup>43,44</sup>. These results indicate that SST-driven atmospheric teleconnections from the Indo-Pacific play a key role in shaping the Antarctic sea ice tripole patterns.

To assess the atmospheric response of Antarctic sea ice to Indo-Pacific SST anomalies, we conducted a set of pacemaker experiments forced by observed SST anomalies in Fig. 3 (see “Pacemaker experiments” in “Methods”). By imposing basin-wide Indo-Pacific SST anomalies on the coupled air-ocean-ice system, these experiments evaluate the integrated remote influence of SST forcing. The simulations (Supplementary Fig. 2) reasonably reproduce the observed Antarctic sea-ice tripole patterns in both

seasons. Minor regional differences are mainly confined to the systematic model bias in sea ice extent and variability<sup>45</sup>. For example, the simulated third center exhibits modest longitudinal shifts, moving westward in both seasons (box III<sub>AWT</sub> and III<sub>AST</sub> in Supplementary Fig. 2) relative to the observed locations (box III<sub>AWT</sub> and III<sub>AST</sub> in Fig. 1d, e).

Although the pacemaker experiments support the combined influence of tropical Indo-Pacific SST variability on Antarctic sea ice tripole patterns, the individual contributions of each basin remain unclear. To isolate these effects, we extracted SST indices from the Indian Ocean (IO), Maritime Continent (MC), and central-Pacific Ocean (PO) regions (green boxes in Fig. 3) of the Indian Ocean (IO), Maritime Continent (MC), and applied Gram–Schmidt orthogonalization to obtain a set of independent SST indices (see “Partial regression analysis” in “Methods”). We then examined how each index influences sea ice and its associated Rossby-wave pathways using observational data (Figs. 4 and 5), and subsequently evaluated these pathways using atmospheric transient experiments (Supplementary Figs. 4 and 5) (see “Atmospheric transient experiments” in “Methods”). In these simulations, SST anomalies associated with each tropical basin are prescribed separately, allowing us to isolate the basin-specific atmospheric forcing responsible for generating distinct Rossby wave trains.

During JJA, we examine the respective impacts of SST variability in the central Pacific and Indian Oceans (Fig. 4). Regressions on 1 °C SST variations show that both the  $PO_{\perp}$  and  $IO_{\perp}$  indices generate tripole-like Antarctic sea-ice patterns (Fig. 4a, c). The  $PO_{\perp}$ -related pattern (Fig. 4a) closely

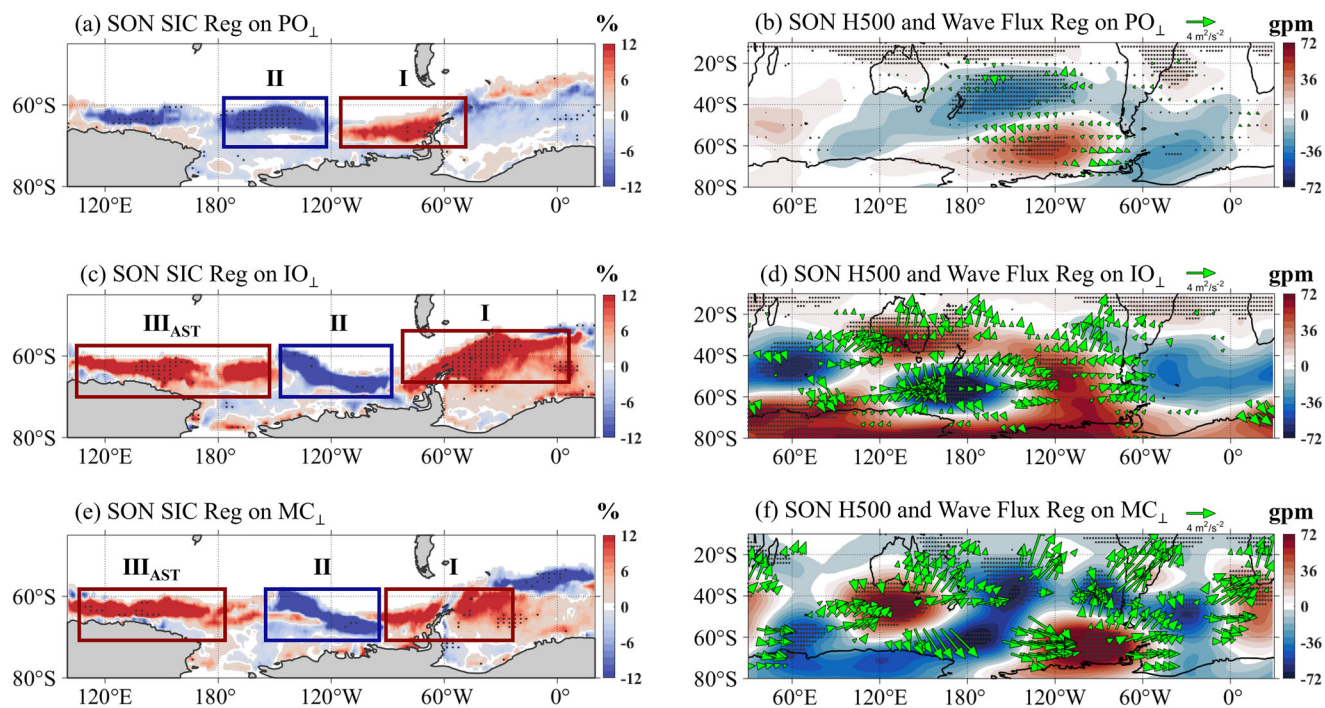


**Fig. 5 | Distinct Rossby wave trains from the Indo-Pacific Oceans modulating the Antarctic sea ice tripole during austral spring.** Partial regressions of (a) SIC (shading) and (b) H500 (shading) and Plumb wave flux (arrows) against the independent  $PO_{\perp}$  index during SON. c–f are the same as a, b, but for the  $IO_{\perp}$  and  $MC_{\perp}$  indices, respectively. The anomalies represent the response to a  $1^{\circ}$  variation in these

SST indices. Stippling represents the areas with statistically significant regression coefficients at a level of  $<5\%$  based on Student’s  $t$ -test. Boxes I–II in (a) show the classic dipole structure under  $PO_{\perp}$  forcing, while the additional box  $III_{AST}$  in (b, c) highlight the emergence of a springtime tripole under  $IO_{\perp}$  and  $MC_{\perp}$  forcing.

matches the leading EOF mode (Fig. 1d), whereas the  $IO_{\perp}$ -related pattern (Fig. 4c) is displaced eastward by  $\sim 20^{\circ}$ , with anomalies concentrated in the Weddell and King Hakon VII Sea (boxes I and  $III_{AST}$  in Fig. 4c). In contrast,  $MC_{\perp}$ -related SST variability during JJA does not generate statistically significant Antarctic sea-ice anomalies or a tripole-like pattern (Supplementary Fig. 3a), consistent with its weak relationship with AWT (Fig. 3a). Accordingly, the following analysis focuses on the  $PO_{\perp}$ - and  $IO_{\perp}$ -related atmospheric responses.

The  $PO_{\perp}$ -induced Rossby wave train (Fig. 4b) originates in the central Pacific, propagates toward Antarctica, weakens the ASL, and deepens the Weddell Sea low, consistent with the local “circulation pairs” (Fig. 2a). This interaction strengthens the tripole structure through local dynamic feedback associated with surface wind anomalies. In contrast, the  $IO_{\perp}$ -induced wave train (Fig. 4d) originates in the southern Indian Ocean and propagates eastward toward the western Ross Sea, where most wave energy reflects back to mid-latitudes, and only a small fraction reaches the Weddell Sea, contributing weakly to tripole formation.

Atmospheric transient experiments confirm this contrast (see “Atmospheric transient experiments” in “Methods”): the  $PO_{\perp}$ -forced simulation (Supplementary Fig. 4a) reproduces the anomalous high over the Amundsen Sea and low over the Weddell Sea observed in reanalysis (Fig. 4b), whereas the  $IO_{\perp}$ -forced simulation (Supplementary Fig. 4b) produces a similar pattern but shifted about  $20^{\circ}$  west of the observed wave path (Fig. 4d). Additionally, the intensity of the simulated response is approximately half of that seen in observations. This discrepancy in strength could stem from limitations in model resolution, which may affect the model’s ability to accurately capture interactions within the subtropical jet and complex wave reflection processes.

In SON, we also examine the Maritime Continent due to its strong negative correlation with the Antarctic sea-ice tripole. Partial regressions of SIC show that patterns linked to the  $IO_{\perp}$  and  $MC_{\perp}$  indexes (boxes I–III in Fig. 5c, e) closely reproduce the observed springtime tripole (boxes I–III in

Fig. 1e). In contrast, the  $PO_{\perp}$ -induced pattern (Fig. 5a) resembles a classic dipole, failing to reproduce the third anomaly center over the Dumont d’Urville Sea (box  $III_{AST}$  in Fig. 1e).

To further understand these differences, we examine the associated Rossby wave trains. The  $IO_{\perp}$ -related Rossby wave train exhibits marked seasonality: in SON, its wave flux (Fig. 5d) intensifies and shifts west of the dateline compared to JJA (Fig. 4d), significantly deepening the low-pressure anomaly over the western Ross Sea and reinforcing the spring tripole (Fig. 5c). In contrast, the  $PO_{\perp}$ -induced wave train maintains a similar structure between JJA (Fig. 4b) and SON (Fig. 5b), but its influence on the Ross and Weddell Seas weakens during SON, particularly over the Ross Sea, which is crucial for tripole formation. The  $MC_{\perp}$ -induced wave train (Fig. 5f) originates from the subtropical eastern Indian Ocean and strengthens the low-pressure anomaly over the western Ross Sea, facilitating the development of the third anomaly center over the Dumont d’Urville Sea (box  $III_{AST}$  in Fig. 5e).

Atmospheric transient experiments further support these findings: the  $IO_{\perp}$ - and  $MC_{\perp}$ -forced simulations (Supplementary Fig. 5b, c) reproduce the observed Rossby wave paths and enhance the western Ross Sea Low, whereas the  $PO_{\perp}$ -forced simulation retains only a limited impact (Supplementary Fig. 5a).

Therefore, partial regression and transient experiments confirm that Rossby wave trains from different basins display contrasting seasonal behavior. To investigate the origin of this contrast, we further analyze the moderating role of the Southern Hemisphere mean flow in shaping Rossby wave trajectories. The subtropical jet (black contours in Fig. 6) forms a broad imaginary wave number region (white zone in Fig. 6) south of the jet core, which acts as a barrier to the wave propagation (see “Rossby wave number” in “Methods”). This barrier strengthens in JJA and weakens in SON. In both seasons, wave activity originating from the central Pacific (red arrows) crosses the barrier-free region and produces the eastern high–low “circulation pair” (red and blue solid circles), thereby contributing efficiently to the winter tripole.

In contrast, the pathways of wave trains originating from the Indian Ocean and Maritime Continent depend strongly on the seasonal configuration of the subtropical jet. During JJA (Fig. 6a), the strengthened barrier deflects Indian Ocean wave activity (blue arrows) past the Ross Sea, allowing it to reach the King Hakon VII Sea, supporting the winter tripole. During SON (Fig. 6b), the barrier contracts westward, allowing wave trains from both the Indian Ocean (blue arrows) and the Maritime Continent (purple arrows) to penetrate the westerlies and reach the western Ross Sea, where they amplify the western low–high “circulation pair” (blue and red solid circles) that characterizes the spring tripole.

In summary, reanalysis data and numerical experiments reveal that Antarctic sea ice tripole patterns result from both combined and basin-specific Indo-Pacific SST effects. The central Pacific dominates in winter, while the Indian Ocean and Maritime Continent prevail in spring. Seasonal shifts in Rossby wave propagation, shaped by background flow and waveguides, drive the shift of the third anomaly center within the tripole.

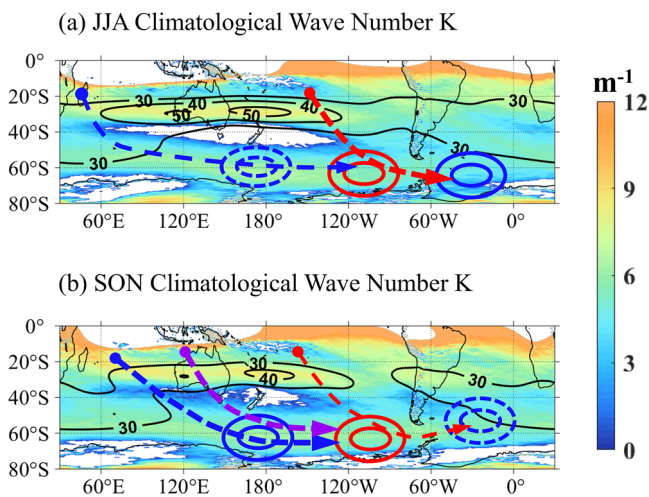


**Fig. 6 | Southern Hemisphere mean flow related to Rossby wave dynamics.** Rossby wave number ( $K$ ) during JJA (a) and SON (b). The black contour represents the mean state of 200-hPa zonal wind speed, which indicates the strength of the subtropical jet. South of the jet, strong zonal wind shear generates regions of negative zonal wind velocity, resulting in areas of imaginary  $K$  (white shading) that act as reflective barriers to wave propagation (see “Rossby wave number” in “Methods”). Colored arrows indicate stationary Rossby wave trains triggered by tropical forcing from the IO (blue), PO (red), and MC (purple). Red (blue) circles denote the anomalous high (low) circulation centers in the “circulation pair.” Solid contours denote circulation anomalies located sufficiently close to the sea ice edge to influence the tripole pattern, whereas dashed contours indicate weaker or more distant anomalies with limited impact.

### Discussion

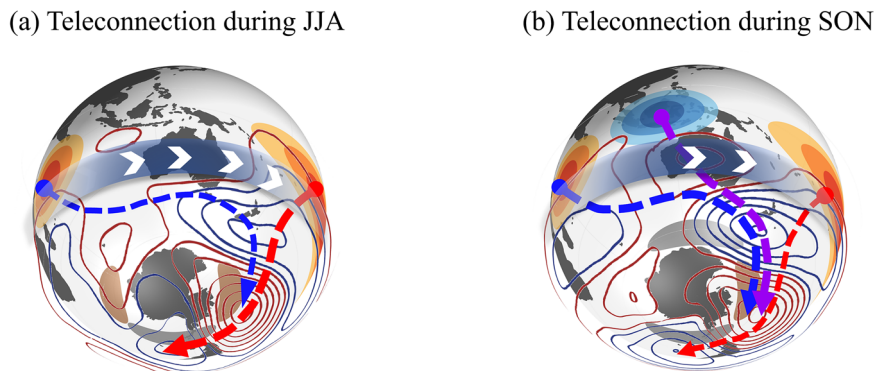
By revealing the tripole-like Antarctic sea ice anomaly patterns (AWT and AST), this work extends the traditional Antarctic Dipole framework to coherent variability across multiple Southern Ocean sectors. A third anomaly center emerges in different regions across seasons—over the King Hakon VII Sea in winter and the Dumont d’Urville Sea in spring (Fig. 7). This highlights a more complex interannual spatial structure of Antarctic sea ice variability than previously recognized.

These tripole patterns are not merely extensions of the ASL-induced dipole but are shaped by “circulation pairs,” whose strong meridional winds cut across dynamically sensitive transitional sea-ice belts, emphasizing the role of regional atmospheric dynamics. These “circulation pairs” are, in turn, modulated by Rossby wave trains excited by tropical SST variability, thereby linking local dynamics to remote tropical forcing. Our results underscore that SST variability across the tropical Indo-Pacific exerts both synergistic and basin-specific influences on Antarctic sea ice through distinct Rossby wave pathways (arrows in Fig. 7). While previous studies have primarily focused on the remote effects of the Pacific<sup>22,29–31</sup> and Atlantic<sup>46–48</sup> on Antarctic sea ice, our analysis reveals a clearer differentiation among the tropical Indo-Pacific regions. The central Pacific dominates the formation of the tripole pattern in winter through robust wave trains, whereas in spring, the Indian Ocean and Maritime Continent emerge as key contributors—particularly in shaping the third anomaly center.

In JJA (Fig. 7a), stationary Rossby wave trains (arrows) triggered by SST warming in the Indian and central Pacific Oceans (orange shading) propagate into Southern Hemisphere mid- to high latitudes and generate paired circulation anomalies around Antarctica (contours). These “circulation pairs” intersect transitional sea ice zones, producing a negative–positive–negative tripole from the Ross to the King Hakon VII Sea (brown–gray–brown shading), driven by thermal advection and mechanical forcing. The subtropical jet (blue belts) regulates the poleward penetration of the wave trains. In SON (Fig. 7b), the weakened subtropical jet (blue belts) allows wave trains from the Indian Ocean (blue arrow) and the Maritime Continent (purple arrow) to intrude more directly into the western Ross Sea. The “circulation pairs” tilts southeastward (contours), supporting a positive–negative–positive tripole from the Dumont d’Urville to the Weddell Sea (gray–brown–gray shading). Together, these results establish a refined physical framework linking tropical Indo-Pacific SST variability to Antarctic sea ice anomalies and highlight the overlooked roles of the Indian Ocean and Maritime Continent teleconnections in Antarctic sea ice predictability.

The classic Antarctic Dipole pattern has been recognized for more than two decades<sup>1,2</sup>, with a primary focus on sea ice variability around West Antarctica. However, sea ice variability over King Hakon VII Sea and Dumont d’Urville Sea exhibits a similar magnitude to that in West Antarctica<sup>3</sup>, yet its structure and driving forces have not received

**Fig. 7 | Schematic diagram of Rossby wave train linking tropical ocean and the Antarctic sea ice tripole.** Arrows indicate wave trains triggered by SST anomalies (warm and cold shading) in the Indian Ocean (blue), central Pacific (red), and Maritime Continent (purple). These wave trains propagate across the subtropical jet (blue contours), interact with high-latitude circulation (red and blue contours around Antarctica), and modulate the spatial structure of sea ice tripole patterns (brown and gray shadings). **a** In austral winter (JJA), central-Pacific SST warming dominates the tripole formation, with supplementary influence from the Indian Ocean. **b** In austral spring (SON), Indian Ocean warming and Maritime Continent cooling become the main drivers.



adequate investigation. One reason this broader tripole-like pattern has not been identified previously is that these East Antarctic centers emerge only during specific seasons. Their sea ice cover becomes sufficiently extensive in winter and spring to support large, coherent anomaly centers, whereas during summer and autumn the reduced ice extent masks this variability<sup>3</sup>. At the same time, the subtropical jet is also strongest and most coherent during JJA and remains organized in SON<sup>26</sup>, forming an efficient waveguide that allows wave activity from tropical oceans to reach Antarctica<sup>36</sup>. In contrast, the weakened summer jet limits Rossby-wave penetration into polar latitudes, and the reduced sea ice extent limits the surface expression of anomalies, suppressing the tripole during DJF and MAM.

The tripole-like pattern identified here emerges from the perspective of sea ice-dominated variability. Although it shares some similarities with the circulation-based zonal wave-3 (ZW3) pattern<sup>49,50</sup>, the two differ fundamentally in their wavenumber characteristics and seasonal behavior. ZW3 is a well-established circulation mode that peaks in austral winter and exhibits a mean longitudinal phase shift of about 20°–40° between seasons<sup>51,52</sup>. It is characterized by six sea-ice anomaly centers around Antarctica, with the strongest three located in West Antarctica, reflecting the enhanced wave-packet amplitude in this region<sup>51</sup>. This circulation-based framework has been highly valuable for understanding how planetary-wave variability imprints on Antarctic sea ice<sup>53</sup>. In contrast, when sea-ice internal variability is used as the organizing perspective, the leading interannual SIC mode neither displays the six-center structure nor shows the seasonally rotating phase that typifies ZW3. Instead, during JJA and SON, it appears as a tripole, with the dipole centers remaining nearly stationary and only the third center shifting between seasons. This behavior indicates that the seasonal differences of the tripole do not arise from a rotating phase but reflect internal sea-ice variability together with seasonally shifting Rossby-wave pathways originating from the Indo-Pacific basins.

Rossby wave dynamics link tropical Indo-Pacific variability with Antarctic circulation pairs, which in turn influence sea ice variability through regional atmosphere-ocean-ice interactions. These mechanisms allow us to establish the seasonal Antarctic sea ice tripole pattern and link it to remote forcing from the tropics. Nevertheless, other regional processes, such as cloud-radiative feedback<sup>54–58</sup>, ice-albedo feedback<sup>59–61</sup>, and ocean dynamical processes<sup>40,62,63</sup> may also contribute to this large-scale variability. The role of these regional processes in the formation of the Antarctic sea ice tripole will be a primary focus of our future studies. On the other hand, the evolving influence of tropical SSTs on the Antarctic sea ice remains an area of concern, particularly under greenhouse warming. Recent studies<sup>42,64</sup> have reported that since the late 1990s, the Antarctic Dipole has weakened in both its spatial structure and its teleconnection with ENSO. These findings underscore the need to investigate the inter-decadal variability of the Antarctic sea ice tripole and disentangle the relative contributions of internal variability and external tropical SST forcing.

This study extends the Antarctic Dipole framework by establishing a continent-wide sea ice pattern, providing a new perspective for understanding sea ice variability across the Southern Ocean and its seasonal characteristics. Furthermore, this study highlights the importance of the Indian Ocean in driving the Antarctic sea ice changes, which has, to some extent, received less attention in the previous literature. The teleconnection between the Indian Ocean and Antarctic sea ice, as well as its co-effects with Pacific-induced teleconnections, may have broader implications for understanding Antarctic climate variability and changes<sup>5,65,66</sup>. Given the extensive simulations and projections of tropical SST variability under multiple future emission scenarios<sup>67–71</sup>, these teleconnection insights offer new potential to improve Antarctic sea ice predictions on decadal time-scales—by linking well-characterized tropical SST signals with high-latitude sea ice responses.

## Methods

### Datasets

For this analysis, we employ multiple observational and reanalysis datasets to ensure robustness and comprehensiveness. SIC and SST data are obtained from the Met Office Hadley Centre Global SST dataset (HadISST)<sup>72</sup>. To further validate the sea ice patterns, additional observational datasets from the National Snow and Ice Data Center (NSIDC)<sup>73</sup> and reanalysis datasets from the European Centre for Medium Range Weather Forecasts (ECMWF) Reanalysis version 5 (ERA5)<sup>74</sup> are utilized. Atmospheric variables, including 2-m air temperature and geopotential height (GPH), and so on, are also sourced from the ERA5 reanalysis dataset. For surface wind stress, we use data from the ECMWF Ocean Reanalysis System version 5 (ORAS5)<sup>75</sup>. The monthly averaged data from March 1979 to February 2023 are used for EOF and regression analysis. Anomalies are computed relative to the 1979–2023 climatological annual cycle, and all fields are detrended at each grid point over the same period.

### EOF analysis

We conduct EOF decomposition on sea ice edge (30% SIC) anomalies (longitude-time dimension) around Antarctic regions to investigate the annual and seasonal sea ice variability<sup>1,2</sup>. We project the SIC anomalies (longitude-latitude-time dimension) onto the first principal component to achieve a two-dimensional spatial distribution of the dominant sea ice variability<sup>42</sup>. The spatial patterns reveal a tripole-like pattern of sea ice during JJA and SON, corresponding to the AWT and AST, with the first principal component serving as the AWT and AST index. The observed tripole-like pattern during austral winter and summer from the HadISST dataset (Fig. 1d, e) is validated using the NSIDC observational datasets (Supplementary Fig. 6a, b) and ERA5 reanalysis datasets (Supplementary Fig. 6c, d).

### Partial regression analysis

To quantify the influence of tropical SST variability on the Antarctic sea ice and circulations, partial regression analyses are conducted for austral winter (JJA) and spring (SON). Three regional SST indices are defined: area-weighted SST averages over the IO region (40°E–110°E, 20°S–10°N; left green boxes in Fig. 3a, b), MC region (100°–160°E, 20°S–10°N; middle green boxes in Fig. 3b) and PO region (180°–120°W, 20°S–10°N; right green boxes in Fig. 3a, b). To maintain consistency in sign interpretation, the MC index is defined as the negative SST anomaly over its domain, thereby reflecting the impact of MC cooling on Antarctic climate. To separate the individual effects of each SST region, the SST indices are orthogonalized using the Gram-Schmidt method<sup>76</sup>. We constructed the independent PO<sub>⊥</sub> index by removing the linear contribution of the IO and MC index from the original PO index. Likewise, the independent IO<sub>⊥</sub> and MC<sub>⊥</sub> indices are constructed by removing the linear contributions of the other two regions. The Student's *t*-test is used to calculate the significance level.

### Plumb wave activity flux

The Plumb wave activity flux<sup>77</sup> can capture stationary Rossby wave activities using quasi-geostrophic assumptions in spherical and log-pressure coordinates. Here, we combine the Plumb wave activity flux with the potential height to investigate the role played by planetary waves in connecting the tropics to the Antarctic, whose horizontal component  $F_H$  is given by

$$F_H = p \cos \varphi \times \begin{bmatrix} v'^2 - \frac{1}{2\Omega R \sin 2\phi} \frac{\partial(v'\phi')}{\partial \lambda} \\ -u'v' + \frac{1}{2\Omega R \sin 2\phi} \frac{\partial(u'\phi')}{\partial \lambda} \end{bmatrix} \quad (1)$$

Where  $p$  = pressure/1000mb;  $\varphi$  and  $\lambda$  are latitude and longitude, respectively;  $u, v$  are the horizontal geostrophic wind;  $\phi$  is the geopotential height;  $\Omega$  is the Earth's rotation rate;  $R$  is the Earth's radius. The prime ( $u', v', \phi'$ ) indicates deviations from the mean state.

### Rossby wave number

The Climatological Rossby wave number<sup>78</sup>  $K$  is determined by the 200hPa planetary vorticity  $\beta$  and the zonal velocity  $U$  of the background flow.

$$K = \sqrt{\frac{\beta - U_{yy}}{U}} \quad (2)$$

Where  $\beta - U_{yy}$  represents the meridional gradient of the absolute vorticity, and when the meridional curvature  $U_{yy}$  is excessively large, the total wave number  $K$  becomes an imaginary, creating a wave barrier that blocks the wave flux and limits the propagation of the Rossby wave train.

### Pacemaker experiments

Pacemaker experiments were conducted using the fully coupled Community Earth System Model (CESM), developed by the National Center for Atmospheric Research (NCAR)<sup>45</sup>. The model configuration corresponds to the F19\_G16 grid, with a horizontal resolution of approximately 1.9° for the atmospheric and land components and ~1.0° for the ocean and sea ice components. Here, CESM is employed as a dynamical framework to examine teleconnection processes, with the pacemaker approach used to isolate the forced response to tropical SST anomalies.

In this experimental framework, SST anomalies over the Indo-Pacific region are imposed via mixed-layer heat flux adjustments, following the Newtonian restoring approach. The temperature in the ocean mixed layer is relaxed toward a prescribed target SST field  $T_r$  using the formulation:

$$F = cD(T_r - T_m)/\tau \quad (3)$$

where  $c$  is the heat content of seawater,  $D$  is the mix-layer depth,  $T_r$  is the restoring target temperature,  $T_m$  is the model temperature at each time step, and  $\tau$  is the restoring timescale, which is set as 5 days in this study.

Three ensemble experiments are conducted: one control run and two perturbed runs (for JJA and SON, respectively). In the control run, the mixed-layer temperature over the tropical oceans (20°S–20°N), with 10° buffer zones on both the northern and southern boundaries, is restored to the climatology state (with 1981 to 2010 full seasonal cycle derived from the HadISST), ensuring the tropical region remains in a neutral state. In the perturbed experiments, SST anomalies derived from regression fields of observed SST against the AWT and AST indices (for JJA and SON, respectively) are superimposed on the model climatology within the same Indo-Pacific region. Buffer zones of 10° width are retained to ensure a smooth transition at the nudging boundaries. The Atlantic basin is always restored to its climatological mean state to exclude potential interference, while other regions remain freely coupled.

Each simulation is integrated for 60 years from identical initial conditions. The first 20 years are discarded as spin-up, and years 21–60 are used for analysis. The sea ice responses to Indo-Pacific SST forcing are diagnosed as the difference between the ensemble mean of each perturbed run and the control run.

### Atmospheric transient experiments

To examine the atmospheric pathways linking tropical SST variability to Southern Hemisphere circulation patterns, we conduct a set of transient experiments using the Community Atmosphere Model version 5 (CAM5)<sup>79</sup>, developed by the National Center for Atmospheric Research (NCAR). CAM5 is the atmospheric component of the Community Earth System Model (CESM) and is configured at a horizontal resolution of 2.5° longitude × 1.9° latitude with 30 vertical levels. It is coupled with the Community Land Model version 4 (CLM4) for land surface processes. Oceanic conditions are prescribed using monthly SSTs from the HadISST datasets.

A 100-year control simulation is first performed using the seasonally varying climatological mean SST and SIC from 1981 to 2010. Twelve years from this control run are randomly selected to initialize 12 ensemble members.

To isolate the atmospheric response to SST variability originating from different parts of the Indo-Pacific, we design three basin-specific experiments targeting the tropical Pacific (20°S–20°N), Indian Ocean (20°S to its northern boundary), and Maritime Continent (20°S–20°N). These non-overlapping domains collectively span the tropical Indo-Pacific, and 5° buffer zones are applied along the adjacent boundaries to ensure smooth dynamical transitions.

Within each experiment, SSTs inside the target basin are replaced by the observed monthly HadISST fields from 1979 to 2023, thereby retaining their full interannual variability. Outside the target basin, SSTs are fixed to the seasonally varying climatological mean (1981–2010) with no interannual variability. This configuration isolates the atmospheric response to SST variability originating solely from the selected basin.

Each ensemble member is integrated from 1979 to 2023, and the 12-member ensemble mean is used to suppress internal atmospheric noise and highlight the forced atmospheric response.

### Data availability

The HadISST data is available at <https://www.metoffice.gov.uk/hadobs/hadisst/data/download.html>. The ERA5 reanalysis data is available at <https://www.ecmwf.int/en/forecasts/datasets/>. The ORAS5 data is available at <https://cds.climate.copernicus.eu/cdsapp#!/dataset/reanalysis-oras5?tab=overview>. The NSIDC observational data is available at <https://nsidc.org/data/g02202/versions/4>. Data to reproduce the figures of this study are provided as Supplementary Data 1.

### Code availability

The data in this study are analyzed with MATLAB, available at <https://in.mathworks.com/products/matlab.html>. The code of the CESM1 model used is available at <http://www.cesm.ucar.edu/models/cesm1.2>. Code to reproduce the figures of this study are provided as Supplementary Data 1.

Received: 26 September 2025; Accepted: 2 February 2026;

Published online: 14 February 2026

### References

1. Yuan, X. & Martinson, D. G. Antarctic sea ice extent variability and its global connectivity. *J. Clim.* **13**, 1697–1717 (2000).
2. Yuan, X. & Martinson, D. G. The Antarctic dipole and its predictability. *Geophys. Res. Lett.* **28**, 3609–3612 (2001).
3. Raphael, M. N. & Hobbs, W. The influence of the large-scale atmospheric circulation on Antarctic sea ice during ice advance and retreat seasons. *Geophys. Res. Lett.* **41**, 5037–5045 (2014).
4. Ma, W., Li, X., Zhang, L., Hou, Y. & Man, K. Sea Ice dipole around East Antarctica induced by remote forcing from Indian Ocean. *J. Geophys. Res. Atmos.* **130**, e2024JD042435 (2025).
5. Zhang, C. & Li, S. Causes of the record-low Antarctic sea-ice in austral summer 2022. *Atmos. Ocean. Sci. Lett.* **16**, 100353 (2023).
6. Zhu, T. & Yu, J. A shifting tripolar pattern of Antarctic sea ice concentration anomalies during multi-year La Niña events. *Geophys. Res. Lett.* **49**, e2022GL101217 (2022).
7. Coggins, J. H. J. & McDonald, A. J. The influence of the Amundsen Sea Low on the winds in the Ross Sea and surroundings: insights from a synoptic climatology. *J. Geophys. Res. Atmos.* **120**, 2167–2189 (2015).
8. Hosking, J. S., Orr, A., Marshall, G. J., Turner, J. & Phillips, T. The influence of the Amundsen-Bellinghousen Seas low on the climate of West Antarctica and its representation in coupled climate model simulations. *J. Clim.* **26**, 6633–6648 (2013).
9. Turner, J., Phillips, T., Hosking, J. S., Marshall, G. J. & Orr, A. The Amundsen Sea low. *Int. J. Climatol.* **33**, 1818–1829 (2013).
10. Holland, M. M., Landrum, L., Raphael, M. N. & Kwok, R. The regional, seasonal, and lagged influence of the Amundsen Sea Low on Antarctic Sea Ice. *Geophys. Res. Lett.* **45**, 11227–11234 (2018).

11. Thompson, D. W. J. & Wallace, J. M. Annular modes in the extratropical circulation. Part I: Month-to-month variability\*. *J. Clim.* **13**, 1000–1016 (2000).
12. Yu, L., Zhong, S., Sui, C. & Sun, B. A regional and seasonal approach to explain the observed trends in the Antarctic sea ice in recent decades. *Int. J. Climatol.* **43**, 2953–2974 (2023).
13. Turner, J., Hosking, J. S., Bracegirdle, T. J., Marshall, G. J. & Phillips, T. Recent changes in Antarctic Sea Ice. *Philos. Trans. R. Soc. Math. Phys. Eng. Sci.* **373**, 20140163 (2015).
14. Liu, J., Yuan, X., Rind, D. & Martinson, D. G. Mechanism study of the ENSO and southern high latitude climate teleconnections. *Geophys. Res. Lett.* **29**, 24-1-24-24-4 (2002).
15. Zhang, C., Li, T. & Li, S. Impacts of CP- and EP-El Niño events on the Antarctic sea ice in austral spring. *J. Clim.* **34**, 1–76 (2021).
16. Hobbs, W. R. & Raphael, M. N. The Pacific zonal asymmetry and its influence on southern hemisphere sea ice variability. *Antarct. Sci.* **22**, 559–571 (2010).
17. Li, X. et al. Tropical teleconnection impacts on Antarctic climate changes. *Nat. Rev. Earth Environ.* **2**, 680–698 (2021).
18. Yuan, X., Kaplan, M. R. & Cane, M. A. The Interconnected global climate system—a review of tropical–polar teleconnections. *J. Clim.* **31**, 5765–5792 (2018).
19. Hoskins, B. J. & Karoly, D. J. The steady linear response of a spherical atmosphere to thermal and orographic forcing. *J. Atmos. Sci.* **38**, 1179–1196 (1981).
20. Jin, D. & Kirtman, B. P. Why the Southern Hemisphere ENSO responses lead ENSO. *J. Geophys. Res. Atmos.* **114**, 2009JD012657 (2009).
21. Simmons, A. J., Wallace, J. M. & Branstator, G. W. Barotropic wave propagation and instability, and atmospheric teleconnection patterns. *J. Atmos. Sci.* **40**, 1363–1392 (1983).
22. Mo, K. C. Relationships between low-frequency variability in the southern hemisphere and sea surface temperature anomalies. *J. Clim.* **13**, 3599–3610 (2000).
23. Clem, K. R., Renwick, J. A. & McGregor, J. Autumn cooling of western East Antarctica linked to the tropical Pacific. *J. Geophys. Res. Atmos.* **123**, 89–107 (2018).
24. Li, X., Gerber, E. P., Holland, D. M. & Yoo, C. A Rossby wave bridge from the tropical Atlantic to West Antarctica. *J. Clim.* **28**, 2256–2273 (2015).
25. Scott Yiu, Y. Y. & Maycock, A. C. On the seasonality of the El Niño teleconnection to the Amundsen Sea region. *J. Clim.* **32**, 4829–4845 (2019).
26. Hoskins, B. J. & Ambrizzi, T. Rossby wave propagation on a realistic longitudinally varying flow. *J. Atmos. Sci.* **50**, 1661–1671 (1993).
27. Kidson, J. W., Revell, M. J., Bhaskaran, B., Mullan, A. B. & Renwick, J. A. Convection patterns in the tropical Pacific and their influence on the atmospheric circulation at higher latitudes. *J. Clim.* **15**, 137–159 (2002).
28. Seager, R., Harnik, N., Kushnir, Y., Robinson, W. & Miller, J. Mechanisms of hemispherically symmetric climate variability. *J. Clim.* **16**, 2960–2978 (2003).
29. Fogt, R. L., Bromwich, D. H. & Hines, K. M. Understanding the SAM influence on the South Pacific ENSO teleconnection. *Clim. Dyn.* **36**, 1555–1576 (2011).
30. L’Heureux, M. L. & Thompson, D. W. J. Observed relationships between the El Niño–Southern oscillation and the extratropical zonal-mean circulation. *J. Clim.* **19**, 276–287 (2006).
31. Turner, J. The El Niño–southern oscillation and Antarctica. *Int. J. Climatol.* **24**, 1–31 (2004).
32. Mo, K. C. & Higgins, R. W. The Pacific–south American modes and tropical convection during the southern hemisphere winter. *Mon. Weather Rev.* **126**, 1581–1596 (1998).
33. Mo, K. C. & Paegle, J. N. The Pacific–south American modes and their downstream effects. *Int. J. Climatol.* **21**, 1211–1229 (2001).
34. Lachlan-Cope, T. & Connolley, W. Teleconnections between the tropical Pacific and the Amundsen-Bellinghousen Sea: role of the El Niño/Southern Oscillation. *J. Geophys. Res. Atmos.* **111**, D23101 (2006).
35. Yu, J.-Y., Paek, H., Saltzman, E. S. & Lee, T. The early 1990s change in ENSO–PSA–SAM relationships and its impact on southern hemisphere climate. *J. Clim.* **28**, 9393–9408 (2015).
36. Li, X., Holland, D. M., Gerber, E. P. & Yoo, C. Rossby waves mediate impacts of tropical oceans on west Antarctic atmospheric circulation in austral winter. *J. Clim.* **28**, 8151–8164 (2015).
37. Zhang, L., Ren, X., Cai, W., Li, X. & Wu, L. Weakened western Indian Ocean dominance on Antarctic sea ice variability in a changing climate. *Nat. Commun.* **15**, 3261 (2024).
38. Nuncio, M. & Yuan, X. The influence of the Indian Ocean dipole on Antarctic Sea Ice\*. *J. Clim.* **28**, 2682–2690 (2015).
39. Dou, J. & Zhang, R. Impact of sea surface temperature in the extratropical southern Indian Ocean on Antarctic sea ice in austral spring. *J. Clim.* **36**, 8259–8275 (2023).
40. Stammerjohn, S., Massom, R., Rind, D. & Martinson, D. Regions of rapid sea ice change: An inter-hemispheric seasonal comparison. *Geophys. Res. Lett.* **39**, 2012GL050874 (2012).
41. Renwick, J. A., Kohout, A. & Dean, S. Atmospheric forcing of Antarctic sea ice on intraseasonal time scales. *J. Clim.* **25**, 5962–5975 (2012).
42. Li, S., Cai, W. & Wu, L. Weakened Antarctic dipole under global warming in CMIP6 models. *Geophys. Res. Lett.* **48**, e2021GL094863 (2021).
43. Zhang, P. & Duan, A. Connection between the tropical Pacific and Indian Ocean and temperature anomaly across West Antarctic. *Npj Clim. Atmos. Sci.* **6**, 49 (2023).
44. Lian, T., Chen, D., Tang, Y. & Jin, B. A theoretical investigation of the tropical Indo-Pacific tripole mode. *Sci. China Earth Sci.* **57**, 174–188 (2014).
45. Hurrell, J. W. et al. The community earth system model: a framework for collaborative research. *Bull. Am. Meteorol. Soc.* **94**, 1339–1360 (2013).
46. Li, X., Holland, D. M., Gerber, E. P. & Yoo, C. Impacts of the north and tropical Atlantic Ocean on the Antarctic Peninsula and sea ice. *Nature* **505**, 538–542 (2014).
47. Ren, X. et al. Influence of tropical Atlantic meridional dipole of sea surface temperature anomalies on Antarctic autumn sea ice. *Environ. Res. Lett.* **17**, 094046 (2022).
48. Simpkins, G. R., Peings, Y. & Magnusdottir, G. Pacific influences on tropical Atlantic teleconnections to the southern hemisphere high latitudes. *J. Clim.* **29**, 6425–6444 (2016).
49. Raphael, M. N. A zonal wave 3 index for the Southern Hemisphere. *Geophys. Res. Lett.* **31**, L23212 (2004).
50. Raphael, M. N. The influence of atmospheric zonal wave three on Antarctic sea ice variability. *J. Geophys. Res. Atmos.* **112**, D12112 (2007).
51. Goyal, R., Jucker, M., Gupta, A. S. & England, M. H. A new zonal wave-3 index for the southern hemisphere. *J. Clim.* **35**, 5137–5149 (2022).
52. Renwick, J. A. Persistent positive anomalies in the southern hemisphere circulation. *Mon. Weather Rev.* **133**, 977–988 (2005).
53. Goyal, R., Jucker, M., Sen Gupta, A., Hendon, H. H. & England, M. H. Zonal wave 3 pattern in the southern hemisphere generated by tropical convection. *Nat. Geosci.* **14**, 732 (2021).
54. Kittel, C. et al. Clouds drive differences in future surface melt over the Antarctic ice shelves. *Cryosphere* **16**, 2655–2669 (2022).
55. Wang, Y., Yuan, X. & Cane, M. A. Coupled mode of cloud, atmospheric circulation, and sea ice controlled by wave-3 pattern in Antarctic winter. *Environ. Res. Lett.* **17**, 044053 (2022).
56. Wang, Y. et al. The contributions of winter cloud anomalies in 2011 to the summer sea-ice rebound in 2012 in the Antarctic. *J. Geophys. Res. Atmos.* **124**, 3435–3447 (2019).

57. Xia, Y. et al. Stratospheric ozone-induced cloud radiative effects on Antarctic Sea Ice. *Adv. Atmos. Sci.* **37**, 505–514 (2020).
58. Yamanouchi, T. & Charlock, T. P. Effects of clouds, ice sheet, and sea ice on the Earth radiation budget in the Antarctic. *J. Geophys. Res. Atmos.* **102**, 6953–6970 (1997).
59. DeConto, R., Pollard, D. & Harwood, D. Sea ice feedback and cenozoic evolution of antarctic climate and ice sheets. *Paleoceanography* **22**, PA3214 (2007).
60. Goosse, H. et al. Quantifying climate feedbacks in polar regions. *Nat. Commun.* **9**, 1919 (2018).
61. Riihelä, A., Bright, R. M. & Anttila, K. Recent strengthening of snow and ice albedo feedback driven by Antarctic sea-ice loss. *Nat. Geosci.* **14**, 832–836 (2021).
62. Beer, E., Eisenman, I., Wagner, T. J. W. & Fine, E. C. A possible hysteresis in the arctic ocean due to release of subsurface heat during sea ice retreat. *J. Phys. Oceanogr.* **53**, 1323–1335 (2023).
63. Wagner, T. J. W., Eisenman, I., Ceroli, A. M. & Constantinou, N. C. How winds and ocean currents influence the drift of floating objects. *J. Phys. Oceanogr.* **52**, 907–916 (2022).
64. Li, S., Cai, W. & Wu, L. Attenuated interannual variability of austral winter Antarctic Sea Ice over recent decades. *Geophys. Res. Lett.* **47**, e2020GL090590 (2020).
65. Purich, A. & England, M. H. Tropical teleconnections to Antarctic Sea ice during austral spring 2016 in coupled pacemaker experiments. *Geophys. Res. Lett.* **46**, 6848–6858 (2019).
66. Wang, G. et al. Compounding tropical and stratospheric forcing of the record low Antarctic sea-ice in 2016. *Nat. Commun.* **10**, 13 (2019).
67. Chen, H. et al. Central-pacific el niño-southern oscillation less predictable under greenhouse warming. *Nat. Commun.* **15**, 4370 (2024).
68. Geng, T. et al. Emergence of changing central-pacific and eastern-pacific El Niño–Southern Oscillation in a warming climate. *Nat. Commun.* **13**, 6616 (2022).
69. Geng, T. et al. Increased occurrences of consecutive La Niña events under global warming. *Nature* **619**, 774–781 (2023).
70. Sharma, S. et al. Future Indian Ocean warming patterns. *Nat. Commun.* **14**, 1789 (2023).
71. Wang, G. et al. The Indian Ocean Dipole in a warming world. *Nat. Rev. Earth Environ.* **5**, 588–604 (2024).
72. Rayner, N. A. et al. Global analyses of sea surface temperature, sea ice, and night marine air temperature since the late nineteenth century. *J. Geophys. Res. Atmos.* **108**, 4407 (2003).
73. Meier, W., Fetterer, F., Windnagel, A. & Stewart, S. NOAA/NSIDC climate data record of passive microwave sea ice concentration, version 4. *Natl. Snow Ice Data Cent.* <https://doi.org/10.7265/efmz-2t65> (2021)
74. Hersbach, H. et al. The ERA5 global reanalysis. *Q. J. R. Meteorol. Soc.* **146**, 1999–2049 (2020).
75. Zuo, H., Balmaseda, M. A., Tietsche, S., Mogensen, K. & Mayer, M. The ECMWF operational ensemble reanalysis–analysis system for ocean and sea ice: a description of the system and assessment. *Ocean Sci.* **15**, 779–808 (2019).
76. Björck, Å Numerics of Gram-Schmidt orthogonalization. *Linear Algebra Appl.* **197–198**, 297–316 (1994).
77. Plumb, R. A. On the three-dimensional propagation of stationary waves. *J. Atmos. Sci.* **42**, 217–229 (1985).
78. Ambrizzi, T., Hoskins, B. J. & Hsu, H.-H. Rossby wave propagation and teleconnection patterns in the austral winter. *J. Atmos. Sci.* **52**, 3661–3672 (1995).
79. Neale, R. B. & Gettelman, A. Description of the NCAR community atmosphere model (CAM 5.0) <https://doi.org/10.5065/wgk-4g06> (2012).

### Acknowledgements

L.Z. is supported by National Key Research and Development Program of China (2023YFF0806700). W.M., Y.H., K.M., Y.M., and X.L. are supported by the National Natural Science Foundation of China (42176243) and the National Science Fund for Distinguished Young Scholars (42325605). X.Y. is supported by a private gift through Lamont-Doherty Earth Observatory (LDEO) of Columbia University.

### Author contributions

X.Y. and L.Z. contributed substantially to the scientific interpretation and mechanistic understanding of the study. W.M. and X.L. conceived and designed all experiments. W.M. and Y.H. performed the pacemaker simulations. W.M. and K.M. conducted the atmospheric transient experiments. W.M. carried out the data analysis and prepared all figures. Y.M. contributed to improving the writing. All authors contributed to reviewing the manuscript.

### Competing interests

The authors declare no competing interests.

### Additional information

**Supplementary information** The online version contains supplementary material available at <https://doi.org/10.1038/s43247-026-03292-7>.

**Correspondence** and requests for materials should be addressed to Li Zhang or Xichen Li.

**Peer review information** : *Communications Earth & Environment* thanks James Renwick and the other, anonymous, reviewer(s) for their contribution to the peer review of this work. Primary Handling Editors: Seung-Ki Min and Nicola Colombo. A peer review file is available.

**Reprints and permissions information** is available at <http://www.nature.com/reprints>

**Publisher's note** Springer Nature remains neutral with regard to jurisdictional claims in published maps and institutional affiliations.

**Open Access** This article is licensed under a Creative Commons Attribution-NonCommercial-NoDerivatives 4.0 International License, which permits any non-commercial use, sharing, distribution and reproduction in any medium or format, as long as you give appropriate credit to the original author(s) and the source, provide a link to the Creative Commons licence, and indicate if you modified the licensed material. You do not have permission under this licence to share adapted material derived from this article or parts of it. The images or other third party material in this article are included in the article's Creative Commons licence, unless indicated otherwise in a credit line to the material. If material is not included in the article's Creative Commons licence and your intended use is not permitted by statutory regulation or exceeds the permitted use, you will need to obtain permission directly from the copyright holder. To view a copy of this licence, visit <http://creativecommons.org/licenses/by-nc-nd/4.0/>.

© The Author(s) 2026